

Accelerating the Pace of Oxygen Evolution Reaction Catalyst Discovery through Megalibraries

Jin Huang,[▽] Zhe Wang,[▽] Jiashun Liang,[▽] Xiao-Yan Li, Jacob Pietryga, Zihao Ye, Peter T. Smith, Alp Kulaksizoglu, Connor R. McCormick, Jaerim Kim, Bosi Peng, Zeyan Liu, Ke Xie, Steven B. Torrisi, Joseph H. Montoya, Gang Wu, Edward H. Sargent,* and Chad A. Mirkin*



Cite This: *J. Am. Chem. Soc.* 2025, 147, 30956–30966



Read Online

ACCESS |



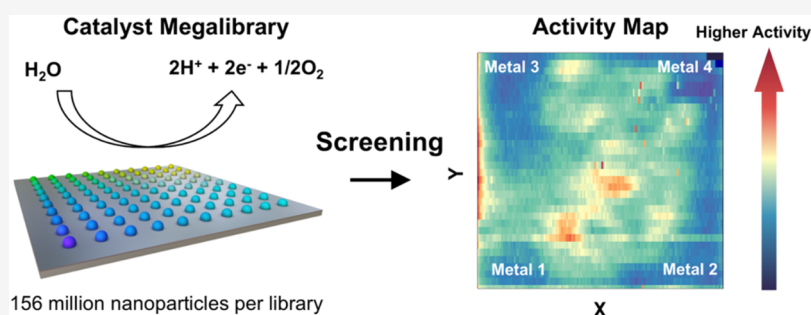
Metrics & More



Article Recommendations



Supporting Information



ABSTRACT: Iridium (Ir) catalysts are essential for the acidic oxygen evolution reaction (OER) in proton-exchange membrane water electrolyzers (PEMWEs), but their high cost, scarcity, and geographical concentration limit large-scale adoption. In addition, the discovery of non-Ir alternatives is slow due to the vast design space possible. Here, a “megalibrary” is used to explore the catalytic activity of ~156 million distinct nanostructures comprised of Ru, Co, Mn, and Cr to find alternatives to Ir catalysts for OER. Over 40 RuCoMnCr oxides, ranging from low to high activity, were selected, scaled to milligram levels, and studied for their catalytic performance. The activities measured within the megalibrary closely correlated ($r = 0.84$) with those of the macroscopic samples. In a PEMWE, the most active catalyst, $\text{Ru}_{52}\text{Co}_{33}\text{Mn}_9\text{Cr}_6$ oxide, demonstrated a voltage of 1.58 V at 1 A/cm² and 1.77 V at 3 A/cm². At 1 A/cm², it operated continuously for over 1000 h with an average voltage increase rate of 57 $\mu\text{V}/\text{h}$. This study establishes a roadmap to accelerate catalyst discovery for energy conversion, and the platform is a route to large data sets that will facilitate the development of AI and machine learning algorithms that can identify key catalyst design features.

INTRODUCTION

A promising approach to contribute to the decarbonization of chemicals and fuels involves the production of hydrogen via water electrolysis using renewable electricity.¹ Proton-exchange membrane water electrolyzers (PEMWEs) produce hydrogen with good energy efficiencies.² However, their rapid scaling is limited by their reliance on IrO_2 as the anodic oxygen evolution reaction (OER) catalyst³ since the global supply of Ir is limited and geographically localized, with >90% in South Africa.⁴ Therefore, there is a need for non-Ir OER catalysts that meet or exceed the activity and stability of IrO_2 . While many advances have been made, the catalysts that have been identified suffer from insufficient activity, stability, or elemental scarcity.⁵ For example, while RuO_2 is more catalytically active than IrO_2 , its low stability makes it a nonviable replacement.⁵ Efforts have been directed toward improving the stability of Ru-based catalysts while maintaining high activity by introducing additional elements (e.g., Co,^{6,7} Ni,⁸ Mn,^{9,10} Cr,¹¹ and Ti¹⁰) or tailoring catalyst morphology,¹² phase,¹³ and structure.^{14–16} The number of possible candidates to be

explored simply through the systematic combination of the elements is daunting, and it is unlikely that optimum structures will be identified serendipitously or through serial methods based on intuition.

Important advances in catalyst discovery have been made through the development of high-throughput techniques,^{17,18} such as thin film deposition¹⁹ and inkjet printing.²⁰ These have typically been limited to 100–25,000 features per library,^{18,21} and the libraries are comprised of features that are highly compositionally variable within a single entity, making it difficult to create scaled up forms that match the properties identified through screening. Recently, we introduced the concept of material megalibraries,²² made possible through a

Received: May 16, 2025

Revised: July 8, 2025

Accepted: July 15, 2025

Published: August 19, 2025



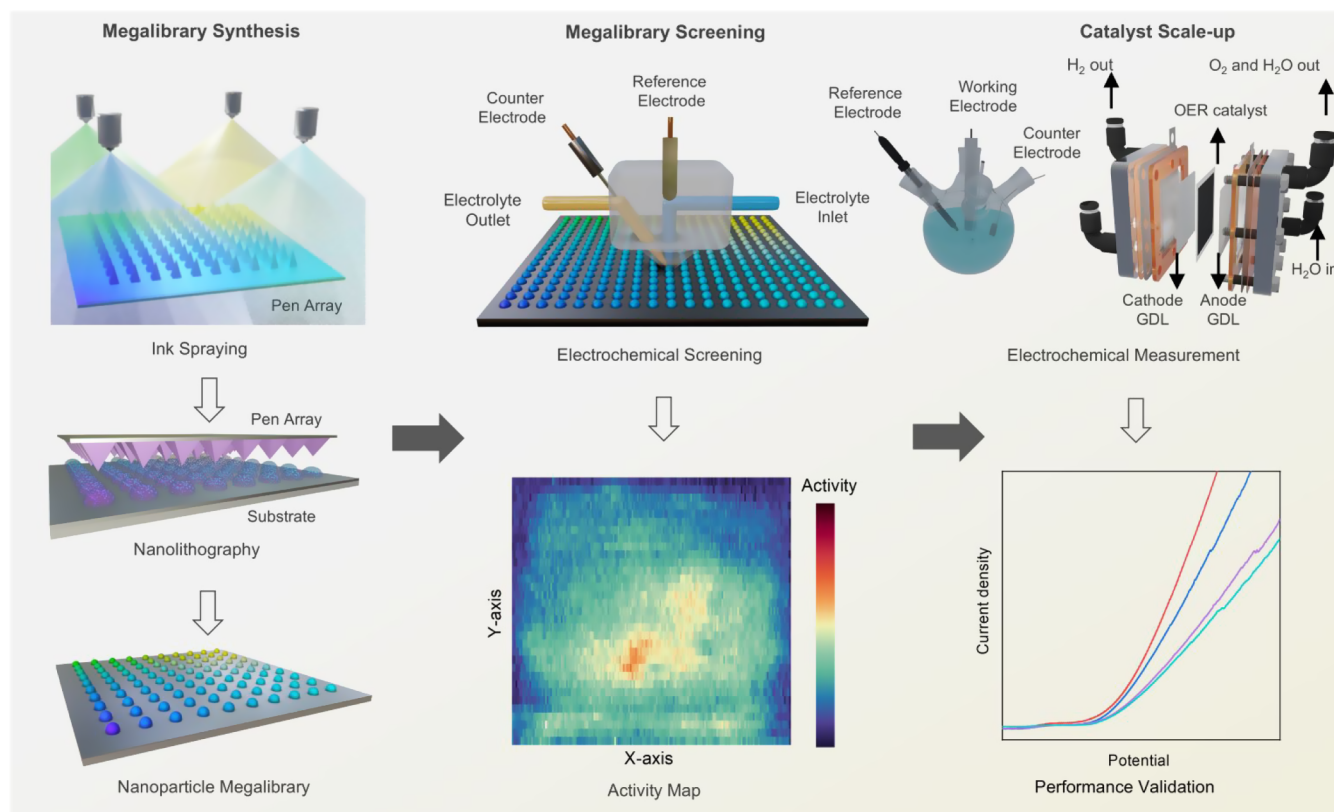


Figure 1. Schematic of the use of megalibrary synthesis, screening, and catalyst scale-up to discover new electrocatalysts. In megalibrary synthesis, nanoreactors with a systematic gradient of elemental precursors (metal salts) are prepared from an ink-coated PPL pen array. The gradient on the array is made via four-nozzle pressurized spraying. After thermally annealing the reactors at 625 °C under H₂ for 6 h and then at 400 °C in air, a nanoparticle megalibrary comprised of 156 million distinct nanoparticles with 250,000 unique composition combinations was formed. Then, scanning droplet cell electrochemistry was used to screen the array for OER activity, yielding an activity map with >5000 data points. Finally, the compositions identified through screening were independently scaled through bulk synthesis and characterized with respect to activity and stability.

combination of polymer pen lithography (PPL)²³ and scanning probe block copolymer lithography (SPBCL).²⁴ Megalibraries consist of hundreds of millions of positionally encoded, well-defined nanostructures (particles) on a surface, allowing one to investigate a much broader parameter set on a 2 cm × 2 cm chip. Each of these particle features is generated from a single attoliter-volume nanoreactor where all of the metal precursors within them are converted into a single particle product. Thus, far, the megalibrary platform has been utilized to identify thermocatalysts for single-walled carbon nanotube growth,²² photocatalysts for pollutant degradation,²⁵ halide perovskites for record blue-light photoluminescence,²⁶ and polyelemental heterostructured materials for a variety of uses, including to enable the acquisition of the massive data sets needed to train machine learning models.²⁷

Herein, we report a four-element (Ru, Co, Mn, and Cr) OER catalyst megalibrary comprised of ~156 million individual nanoparticles with 250,000 unique chemical compositions on a 4 cm² chip. These elements were chosen because they are more abundant and lower in cost than Ir. They have been utilized in other bimetallic OER catalyst studies^{6,7,9,11,28} that identified materials with enhanced activities or stabilities but did not identify clear candidates that could comprehensively compete with IrO₂. Scanning electrochemical methods were used to screen the megalibrary for high-performance OER catalysts (Figure 1). From this analysis, Ru₅₂Co₃₃Mn₉Cr₆ oxide emerged as the most active OER catalyst. Importantly, quantitative activity measurements

of scaled-up forms of the catalyst out-performed those of both RuO₂ and IrO₂. Ru₅₂Co₃₃Mn₉Cr₆ oxide exhibited exceptional activity and stability in membrane electrode assembly (MEA) tests for practical PEMWE applications.

RESULTS AND DISCUSSION

Synthesis and Screening of a RuCoMnCr Oxide Electrocatalyst Megalibrary. A RuCoMnCr oxide OER catalyst megalibrary was synthesized using a PPL-enabled SPBCL method²⁵ (see Supporting Information). In a typical experiment, a polymer pen array containing 250,000 pen tips separated by 30 μm was spray-coated with a quaternary ink gradient composed of Ru, Co, Mn, and Cr metal salt precursors and a poly(ethylene oxide)-*b*-poly(2-vinylpyridine) (PEO-*b*-P2VP) block copolymer and used to pattern nanoreactors onto a glassy carbon (GC) substrate (Figures 1 and 2a). The reactors were thermally annealed at 625 °C under H₂ for 6 h, and the morphology and size of the resulting nanoparticles were characterized using scanning electron microscopy (SEM) and atomic force microscopy (AFM), which indicated that the as-synthesized nanoparticles were predominately single particle structures (>95% yield) (Figure S1). In the four quadrants of the megalibrary, the average size of nanoparticles was 17 ± 3 nm for the Ru-rich region, 15 ± 3 nm for the Co-rich region, 15 ± 3 nm for the Mn-rich region, and 14 ± 3 nm for the Cr-rich region (Figure S1e–h). Finally, air oxidation at 400 °C was used to transform the RuCoMnCr nanoparticle megalibrary into a RuCoMnCr oxide nanoparticle

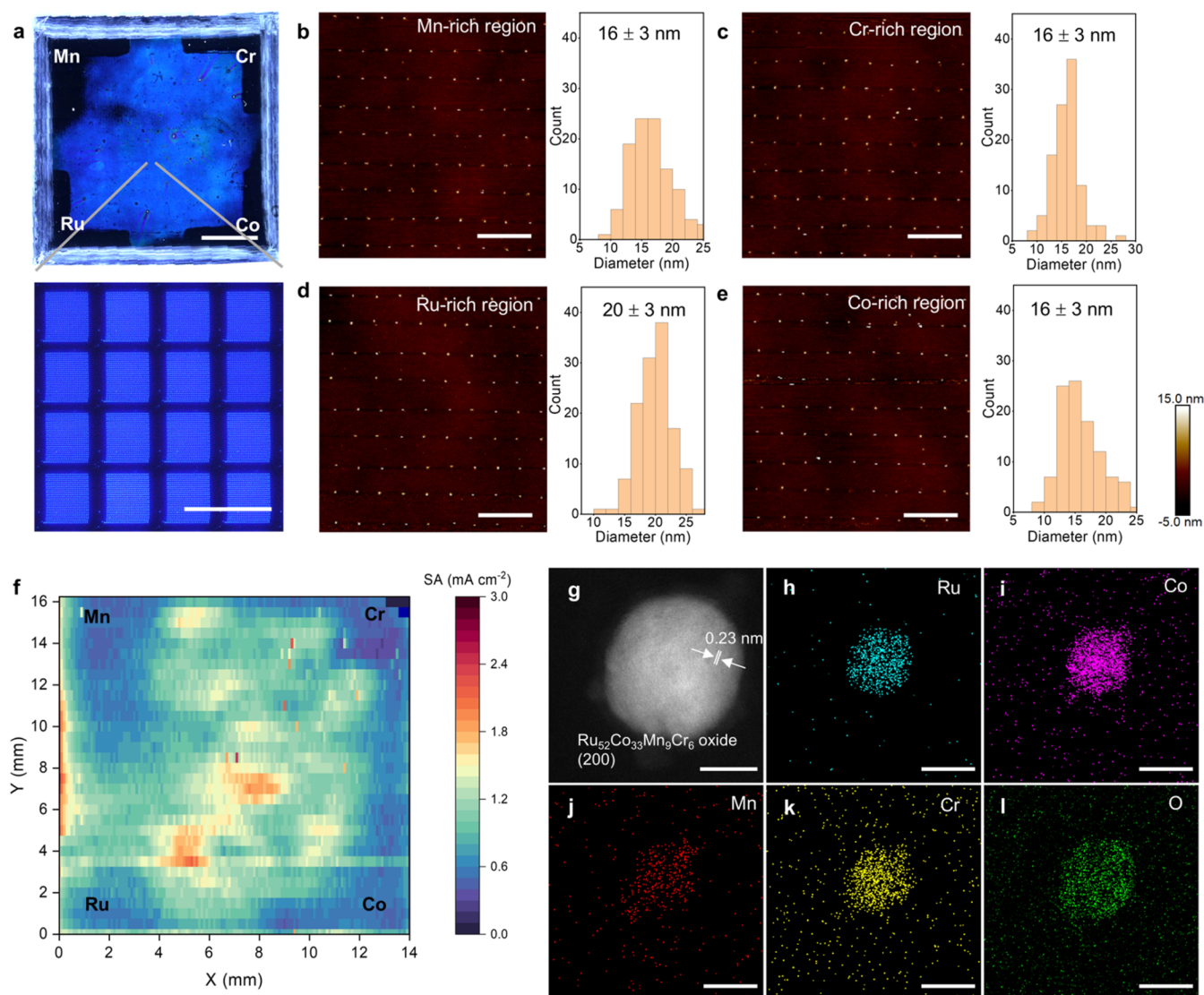


Figure 2. RuCoMnCr oxide megalibrary synthesis, characterization, and electrochemical screening. (a) Optical image of nanoreactors patterned on a polystyrene film-coated GC substrate. Scale bars = 5 mm (top) and 50 μm (bottom). (b–e) AFM height images of a metal oxide nanoparticle array at selected regions (single particle yield >95%) and corresponding statistical analysis. Scale bars = 2 μm. (f) OER SA mapping of a representative RuCoMnCr oxide megalibrary measured in 0.5 M H₂SO₄ at 1.7 V versus RHE. (g) Representative high-resolution HAADF-STEM image of a Ru₅₂Co₃₃Mn₉Cr₆ oxide catalyst. The plane spacing of 0.23 nm corresponds with the (200) facet of Ru₅₂Co₃₃Mn₉Cr₆ oxide. Scale bar = 5 nm. (h–l) Corresponding EDX elemental mapping of Ru₅₂Co₃₃Mn₉Cr₆ oxide nanoparticle. Scale bar = 10 nm.

megalibrary (confirmed by scanning transmission electron microscopy (STEM), *vide infra*). The nanoparticles remained intact after the oxidation process, and the particle sizes slightly increased to 20 ± 3 nm, 16 ± 3 nm, 16 ± 3 nm, and 16 ± 3 nm for the Ru-, Co-, Mn-, and Cr-rich regions respectively (Figures 2b–e and S2); we attribute this result to nanoparticle lattice expansion due to oxygen incorporation.

To rapidly identify the high-activity compositional candidates, we used an automated programmable scanning electrochemical method to measure OER activity. Specifically, a customized scanning droplet cell (SDC)²⁰ (Figure 1) containing a reference electrode (saturated calomel electrode), a counter electrode (graphite), and a flowing electrolyte (0.5 M H₂SO₄, Ar-saturated) was moved laterally across the megalibrary (the working electrode). During scanning, a 500-μm diameter electrolyte droplet with a 1.27% atomic screening resolution (see Supporting Text) was created at the SDC opening to perform serial measurements of electrochemical

signals. To evaluate OER activity, cyclic voltammetry (CV) experiments at four different scan rates over a nonfaradaic region (0.9–1.0 V vs the reversible hydrogen electrode (RHE)) were first performed to determine the electrochemically active surface area (ECSA) across the whole chip (Figures S3 and S4b). To measure the catalytic activity and produce catalytic current maps, the SDC head was subsequently scanned across the megalibrary at a slower velocity (300 μm/s) and at a constant applied potential of 1.7 V vs RHE (Figure S4a). To analyze the data, the background current of the bare GC was subtracted from the catalytic current, and the current was normalized with ECSA to generate a final specific activity (SA) map (Figure 2f).

By comparing the optical image of the GC substrate after PPL and electrochemical measurements (Figure S4d,e), we identified the region with the highest activity on the SA map. The elemental composition at a given position on the megalibrary was determined based on established methods²⁵

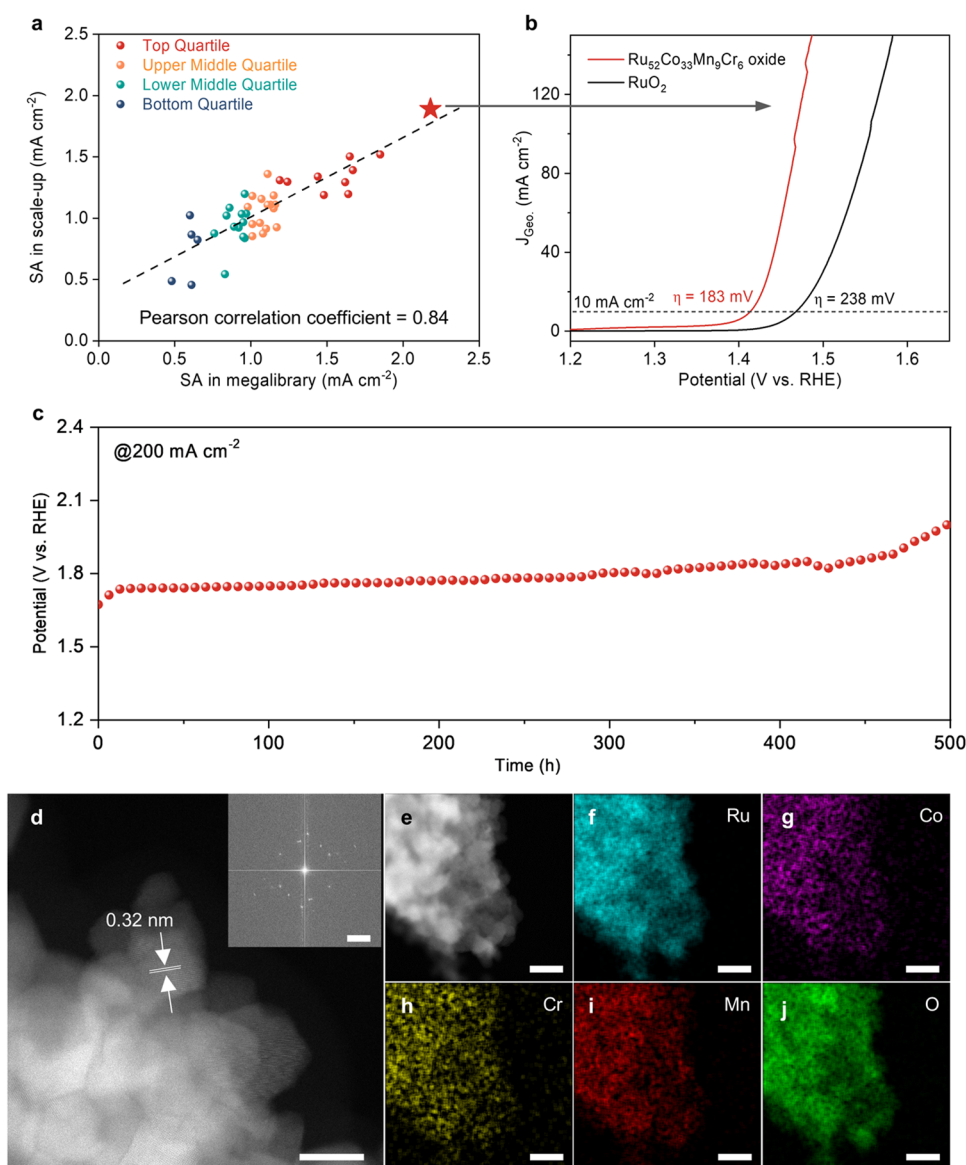


Figure 3. OER performance analysis of $\text{Ru}_{52}\text{Co}_{33}\text{Mn}_9\text{Cr}_6$ oxide catalyst prepared at mg-scale in three-electrode cell. (a) Experimental validation of the SA obtained from megalibrary screening at four different activity levels: top quartile, upper middle quartile, lower middle quartile, and bottom quartile. (b) OER polarization curves of scaled-up $\text{Ru}_{52}\text{Co}_{33}\text{Mn}_9\text{Cr}_6$ oxide and commercial RuO_2 measured on Ti felt. (c) Potential as a function of time (stability) for the $\text{Ru}_{52}\text{Co}_{33}\text{Mn}_9\text{Cr}_6$ oxide catalyst at 200 mA cm^{-2} (uncompensated resistance) on Ti felt. The drop in potential at 420 h is due to the addition of water. (d) Representative high-resolution HAADF-STEM image of the $\text{Ru}_{52}\text{Co}_{33}\text{Mn}_9\text{Cr}_6$ oxide catalyst after acid leaching and electrochemical measurements. Inset: the corresponding fast Fourier transform (FFT) diffraction pattern. Scale bars = 10 and 2 nm^{-1} for inset, respectively. (e–j) HAADF-STEM image and corresponding EDX elemental mapping of $\text{Ru}_{52}\text{Co}_{33}\text{Mn}_9\text{Cr}_6$ oxide after acid leaching and electrochemical measurements. Scale bar = 50 nm.

that rely on energy-dispersive X-ray spectroscopy (EDX) and inductively coupled plasma mass spectrometry (ICP-MS). Through this process, two highly active regions were observed (Figure S4c). On average, these regions corresponded to $\text{Ru}_{52}\text{Co}_{33}\text{Mn}_9\text{Cr}_6$ oxide and $\text{Ru}_{29}\text{Co}_{35}\text{Mn}_{16}\text{Cr}_{20}$ oxide compositions, with $\text{Ru}_{52}\text{Co}_{33}\text{Mn}_9\text{Cr}_6$ oxide showing the highest OER activity; thus, $\text{Ru}_{52}\text{Co}_{33}\text{Mn}_9\text{Cr}_6$ oxide was chosen for comprehensive structural and electrochemical characterization.

Structural and Compositional Characterization of Catalyst Candidates. Since it is challenging to characterize directly the structure of nanoparticles in a megalibrary due to the thickness of the GC substrate, we synthesized $\text{Ru}_{52}\text{Co}_{33}\text{Mn}_9\text{Cr}_6$ oxide nanoparticles on a silicon nitride membrane via SPBCL and dip-pen nanolithography

(DPN)²⁹ for high-angle annular dark-field STEM (HAADF-STEM) and EDX characterization. After we annealed the patterned nanoreactors on the membrane under H_2 , the $\text{Ru}_{52}\text{Co}_{33}\text{Mn}_9\text{Cr}_6$ nanoparticles were determined to be similar in size to that of the particles synthesized via PPL (Figure S5). HAADF-STEM imaging revealed a lattice spacing of 0.21 nm, which corresponds to a (200) facet of $\text{Ru}_{52}\text{Co}_{33}\text{Mn}_9\text{Cr}_6$ metallic nanoparticles. The STEM-EDX mapping revealed that Ru, Co, Mn, and Cr were distributed uniformly throughout the nanoparticles (Figures S6 and S7). A native metal oxide shell was observed on the nanoparticle surface, which can be attributed to the high reactivity of Co, Mn, and Cr metals, which oxidize upon exposure to air (Figure S6f). Upon oxidation in air at 400°C , the nanoparticle structures

and elemental distributions changed; oxygen diffuses into the core of the nanoparticle leading to a lattice expansion (from 0.21 to 0.23 nm) (Figure 2g), indicative of a metal-to-metal oxide transformation (Figures 2h–l and S8). After 4 CV cycles and subsequent OER measurements using chronoamperometry (CA), no detectable changes in morphology were observed (Figures S9–S11).

OER Catalyst Scale-Up Synthesis and Activity Validation. To determine whether the catalyst activity observed in the megalibrary correlates with that of the comparable materials synthesized using a simple spray-annealing method (see Supporting Information), we synthesized catalysts on Ti felt with a loading of approximately 1.5 mg/cm² and performed electrochemical measurements. To assess activity correlation, we sampled 43 catalysts across the four SA quantiles (top quartile, upper middle quartile, lower middle quartile, and bottom quartile) identified during megalibrary screening (Table S1). Importantly, to avoid researcher bias, we used an algorithm to make the selections (see Supporting Information). The algorithm-chosen compositions were then synthesized via direct precursor spray coating on a Ti felt electrode, followed by annealing in air at 400 °C for 1 h (see Supporting Information). The Ti felt was used as the electrode support because it is used as the anode gas diffusion layer in PEMWEs. The SAs of these samples at 1.7 V vs RHE were measured in a typical three-electrode setup, using a Pt coil as the counter electrode and Ag/AgCl as the reference electrode (Figures S12 and S13). The SAs of these 43 as-synthesized catalysts showed a strong linear correlation with the SAs determined from the megalibrary screening (Pearson $r = 0.84$) (Figure 3a) despite the fact that these catalysts were prepared using different synthetic methods, have different catalyst loadings and substrate electrodes, and were analyzed using different measurement methods. Taken together, the results indicate that the activities of the megalibrary catalysts and the scaled-up catalysts correlate well with one another.

The most active catalyst, Ru₅₂Co₃₃Mn₉Cr₆ oxide, exhibited an overpotential of 183 mV at a geometric current density of 10 mA/cm² (Figure 3b), which is 55 mV lower than the overpotential of RuO₂ prepared using the same method. The overpotential of Ru₅₂Co₃₃Mn₉Cr₆ oxide was only 236 mV at 100 mA/cm² on the Ti felt working electrode (Figure 3b). The activity of Ru₅₂Co₃₃Mn₉Cr₆ oxide competed favorably with that reported for state-of-the-art Ru- and Ir-based OER electrocatalysts in acid (Table S2). We also performed X-ray photoelectron spectroscopy (XPS) to study the near-surface oxidation states of the catalyst elements (Figures S14–S17). The near-surface composition of the metallic elements is Ru₄₇Co₃₇Mn₁₀Cr₆ (Figure S14). Due to the overlap of Ru 3d and C 1s peaks, Ru 3p peaks were used for analysis. The Ru peaks at 463.0 and 485.4 eV were assigned to Ru⁴⁺ 3p_{3/2} and Ru⁴⁺ 3p_{1/2}, respectively. The Co 2p peaks were deconvoluted into three sets of peaks (779.6 and 795.0 eV, 781.5 and 797.3 eV, and 785.3 and 803.0 eV), corresponding to Co³⁺, Co²⁺, and satellite peaks, respectively. Although the chemical states of Mn were difficult to determine due to the low concentration and the very similar binding energies of Mn²⁺ 2p_{3/2}, Mn³⁺ 2p_{3/2}, and Mn⁴⁺, the energy level splitting (4.7 eV) of the Mn 3s peaks³⁰ indicated that the Mn is mostly Mn⁴⁺. The Cr 2p_{3/2} peak was deconvoluted into peaks from Cr⁶⁺ (577.9 eV) and Cr³⁺ (575.5 eV).

The durability of Ru₅₂Co₃₃Mn₉Cr₆ oxide as an acidic OER electrocatalyst in a three-electrode cell was evaluated through

chronopotentiometry (CP) measurements at a current density of 200 mA/cm² in 0.5 M H₂SO₄ electrolyte (Figure 3c). The Ru₅₂Co₃₃Mn₉Cr₆ oxide catalyst showed remarkable stability, maintaining a steady potential for 500 h. In contrast, the OER stability of most Ru-based electrocatalysts is typically measured at 10 mA/cm² in the tens of hours.⁵ Only a few Ru-based catalysts are capable of sustaining anodic current densities above 100 mA/cm² (Table S2). The ECSA of the catalyst retained 90.6% of its initial value after stability testing (Figure S13d,e). The chemical states of metal elements remained largely unchanged, with more Co oxidized to Co³⁺ according to XPS analysis (Figures S16 and 17 and Table S3). However, we observed changes in the surface composition to Ru₅₆Co₂₈Mn₁₀Cr₆, likely due to Co leaching during the OER process (Figure S16). The chemical states of metal elements remained unchanged according to the XPS analysis (Figures S16 and 17). However, we observed change in the surface composition to Ru₅₆Co₂₈Mn₁₀Cr₆, likely due to Co leaching during the OER process. We also performed ICP-MS analysis to evaluate the stability number of the Ru₅₂Co₃₃Mn₉Cr₆ oxide (Figure S18). The catalyst exhibited a high stability number of approximately 10⁶, which is comparable to, or even exceeds, that of some Ir-based oxide catalysts.³¹

To enable more extensive characterization and a PEMWE study, we scaled up the synthesis of Ru₅₂Co₃₃Mn₉Cr₆ oxide catalysts using a sol–gel method³² and compared the structures of the particle products of this reaction with those of analogous nanoparticles synthesized using SPBCL and DPN methods. X-ray diffraction (XRD) analysis of the sol–gel synthesized Ru₅₂Co₃₃Mn₉Cr₆ oxide catalysts confirmed that they adopt a rutile structure. The calculated grain size, based on the Scherrer equation, was 11.2 nm (Figure S19). The SEM-EDX results showed that the metallic elemental composition of the as-synthesized catalyst was Ru₅₂Co₃₃Mn₉Cr₆, consistent with the composition identified during the megalibrary screening (Figure S20). We characterized the catalysts after acid leaching and electrochemical measurements, as these samples represent the actual catalysts under OER operating conditions (Figure 3d–j). Based on SEM-EDX analysis, the composition shifted to Ru₇₆Co₉Mn₁₁Cr₄ after acid leaching and electrochemical measurements (Figure S21). STEM images showed that the particles are uniform in size (between 11 and 14 nm, Figure 3d,e) and comparable to particles prepared by PPL (Figure 2b–e), and HR-HAADF-STEM analysis revealed a plane spacing of 0.32 nm, corresponding to the (110) facets of rutile phase RuO₂ (Figure 3d). The fast Fourier transform (FFT) (inset of Figure 3d) indicated the existence of Ru₅₂Co₃₃Mn₉Cr₆ oxide (200) and (211) facets with a plane spacing of 0.23 and 0.17 nm, respectively. EDX analysis and line scan results showed uniform distributions of Ru, Co, Mn, and Cr across the sample (Figures 3e–j and S22), consistent with the megalibrary results (Figure 2h–l). We conducted X-ray absorption spectroscopy (XAS) experiments to characterize the fine structure of the Ru₅₂Co₃₃Mn₉Cr₆ oxide catalyst (Figure S23 and Table S4). The Ru–O bond length was found to be 1.97 Å, identical to that of RuO₂, suggesting that no global strain is present in the structure. The enhanced activity and stability are likely attributed to the multielemental oxide surface.

OER Catalytic Reaction Pathway and Computational Study. To investigate the activity and stability of the Ru₅₂Co₃₃Mn₉Cr₆ oxide catalyst, we conducted *operando*

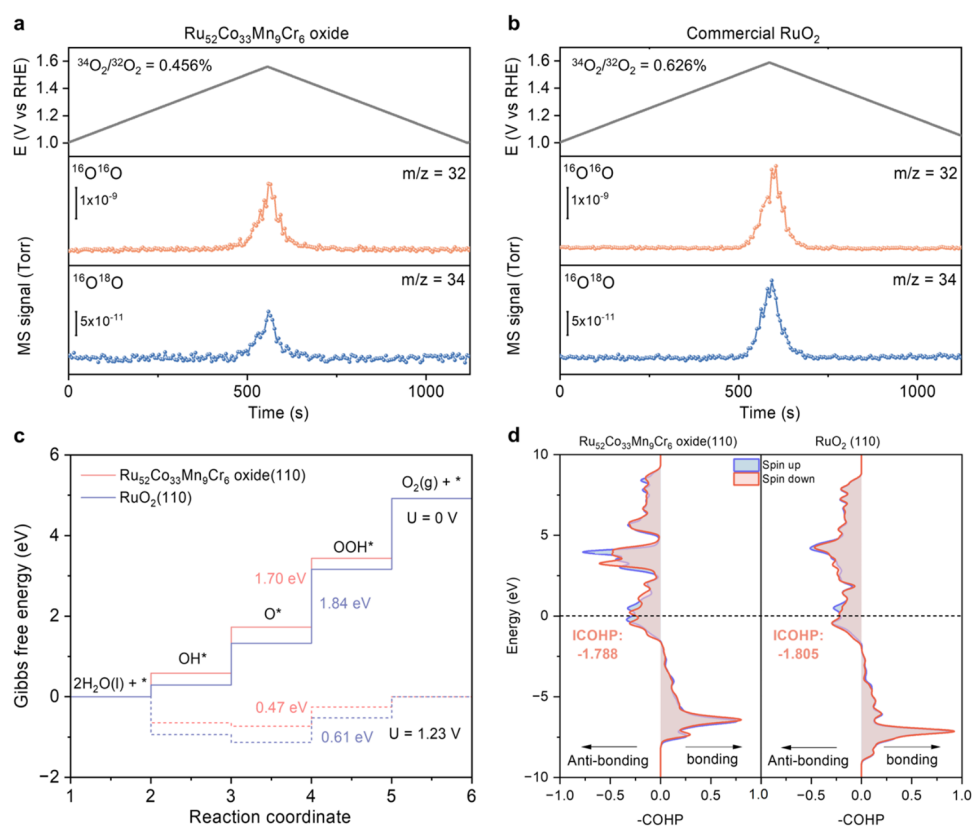


Figure 4. DEMS analysis and DFT calculations of $\text{Ru}_{52}\text{Co}_{33}\text{Mn}_9\text{Cr}_6$ oxide catalyst product distribution. (a, b) DEMS signals under applied potential for $^{32}\text{O}_2$ ($^{16}\text{O}^{16}\text{O}$, mass/charge ratio (m/z) = 32) and $^{34}\text{O}_2$ ($^{16}\text{O}^{18}\text{O}$, m/z = 34) from the gaseous products for ^{18}O -labeled (a) $\text{Ru}_{52}\text{Co}_{33}\text{Mn}_9\text{Cr}_6$ oxide and (b) commercial RuO_2 . The ^{18}O -labeled catalysts were scanned in a normal H_2 / ^{16}O -supported 0.5 M H_2SO_4 electrolyte at a scan rate of 1 mV/s from 1 V vs RHE until the current density reached 20 mA/cm 2 . (c) The free energy diagrams for OER on $\text{Ru}_{52}\text{Co}_{33}\text{Mn}_9\text{Cr}_6$ oxide(110) and RuO_2 (110) surfaces. (d) Average COHP of the lattice Ru–O bond for $\text{Ru}_{52}\text{Co}_{33}\text{Mn}_9\text{Cr}_6$ oxide(110) and RuO_2 (110) surfaces.

differential electrochemical mass spectrometry (DEMS) analysis using an ^{18}O isotope-labeling method.³³ The catalyst surface was first labeled with ^{18}O isotopes by performing CV cycles in 0.5 M H_2SO_4 electrolyte prepared in H_2^{18}O . Subsequently, the isotopic signal of O_2 generated during the OER process was monitored in real time using DEMS while CV in 0.5 M $\text{H}_2\text{SO}_4/\text{H}_2^{16}\text{O}$ electrolyte was conducted (Figure 4a,b). If the oxygen was from the lattice oxygen during the OER, $^{34}\text{O}_2$ would be generated through a combination of ^{18}O from the labeled lattice oxygen and ^{16}O from the electrolyte. The $\text{Ru}_{52}\text{Co}_{33}\text{Mn}_9\text{Cr}_6$ oxide catalyst exhibits a small signal ratio of $^{34}\text{O}_2/^{32}\text{O}_2$ of 0.456%, which is lower than that of commercial RuO_2 (0.626%), indicating suppression of lattice oxygen evolution. Repeated experiments yielded consistent results, with a small relative error of less than 6% (Figure S24).

To gain additional insight into the chemical origins of $\text{Ru}_{52}\text{Co}_{33}\text{Mn}_9\text{Cr}_6$ oxide catalyst activity and stability, we performed density functional theory (DFT) calculations. By evaluating the dopant distributions within the bulk material, we first identified the most stable (110) slab based on a rutile bulk structure model with the composition of $\text{Ru}_{52}\text{Co}_{33}\text{Mn}_9\text{Cr}_6$ oxide, which closely matches the experimentally synthesized composition (Figures S25 and S26). Free energy diagrams for the OER via the O adsorbate evolution pathway were computed for both the $\text{Ru}_{52}\text{Co}_{33}\text{Mn}_9\text{Cr}_6$ oxide(110) and RuO_2 (110) surfaces (Figures 4c, S27, and S28). The formation of $^*\text{OOH}$ from $^*\text{O}$ was identified as the potential-determining step with an energy barrier of 1.70 eV for $\text{Ru}_{52}\text{Co}_{33}\text{Mn}_9\text{Cr}_6$

oxide compared to 1.84 eV for RuO_2 . The $\text{Ru}_{52}\text{Co}_{33}\text{Mn}_9\text{Cr}_6$ oxide(110) surface showed enhanced activity with an overpotential of 0.47 V (at the theoretical thermodynamic potential of 1.23 V versus the standard hydrogen electrode (SHE)). This enhanced activity can be explained using the projected density of states of the Ru 4d orbital (Figure S29). The d-band center of $\text{Ru}_{52}\text{Co}_{33}\text{Mn}_9\text{Cr}_6$ oxide is down-shifted relative to RuO_2 , indicating weaker chemical bonding between the active Ru sites and adsorbed oxygen intermediates³⁴ and leading to a reduced overpotential and a higher OER activity. We further investigated the origin of the catalytic stability by calculating the crystal orbital Hamilton population (COHP). The average integrated COHP for the lattice Ru–O bond in the $\text{Ru}_{52}\text{Co}_{33}\text{Mn}_9\text{Cr}_6$ oxide is -1.788 eV on average (Figures 4d and S30), lower than that of the lattice Ru–O bond in RuO_2 (-1.805 eV) (Figure S31). This reduction in covalency corresponds to a more ionic bonding character, which suppresses oxygen vacancy formation and contributes to the lattice oxygen stabilization.^{35,36} These calculations reveal that optimized interactions between Ru and adsorbed oxygen intermediates and slightly reduced Ru–O covalency are key to simultaneously enhancing the OER activity and stability of $\text{Ru}_{52}\text{Co}_{33}\text{Mn}_9\text{Cr}_6$ oxide catalysts. We note that our current *ex situ* theoretical calculations are primarily intended to provide qualitative insights in support of experimental observations. To further bridge the gap between theory and experiment, more quantitative and advanced modeling approaches such as machine learning potentials or *ab initio* molecular dynamics

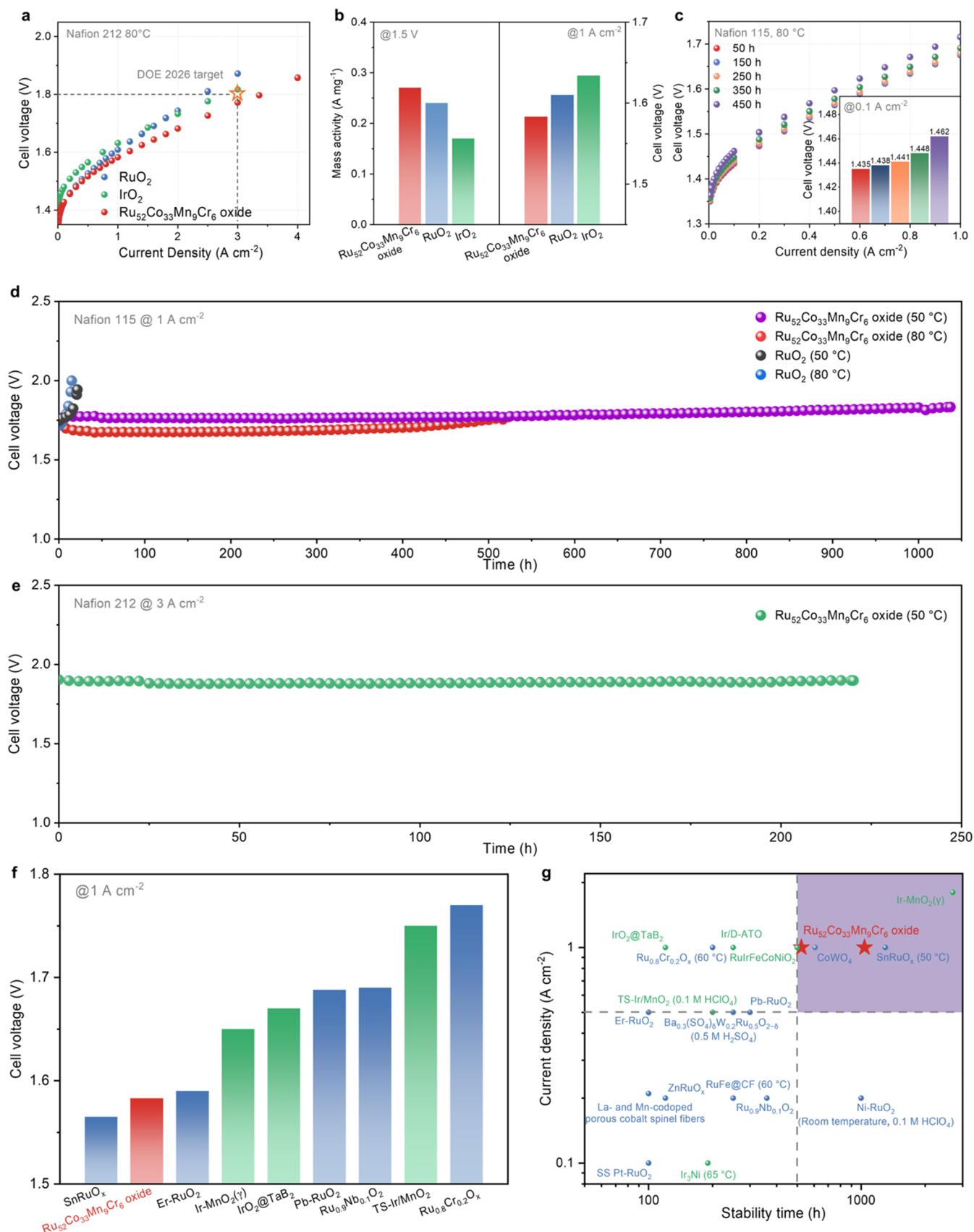


Figure 5. PEMWE studies of Ru₅₂Co₃₃Mn₉Cr₆ oxide catalyst. (a) Polarization curves of Ru₅₂Co₃₃Mn₉Cr₆ oxide, homemade RuO₂, and commercial IrO₂ in PEMWEs at 80 °C. (b) Performance comparison of Ru₅₂Co₃₃Mn₉Cr₆ oxide, RuO₂, and IrO₂ in PEMWEs. (c) Polarization curves of Ru₅₂Co₃₃Mn₉Cr₆ oxide during the stability test at 1 A cm⁻² at 80 °C. The inset displays the potential at 0.1 A cm⁻² over varying operation durations. (d) Stability tests of RuO₂ and Ru₅₂Co₃₃Mn₉Cr₆ oxide at 50 and 80 °C at the current density of 1 A cm⁻². (e) Stability tests of

Figure 5. continued

Ru₅₂Co₃₃Mn₉Cr₆ oxide at 50 °C at the current density of 3 A cm⁻². (f) Cell voltage comparison of Ru₅₂Co₃₃Mn₉Cr₆ oxide with the state-of-the-art catalysts in PEMWEs: SnRuO_x,³⁹ Er-RuO₂,⁴⁰ Ir-MnO₂(γ),⁴¹ IrO₂@TaB₂,⁴² Pb-RuO₂,⁴³ Ru_{0.9}Nb_{0.1}O₂,³² TS-Ir/MnO₂,⁴⁴ Ru_{0.8}Cr_{0.2}O_x,³³ Green markers represent Ir-based catalysts and blue markers represent non-Ir-based catalysts. (g) Stability comparison (combined working current density and working time) between Ru₅₂Co₃₃Mn₉Cr₆ oxide and reported acidic OER electrocatalysts in PEMWEs: Pb-RuO₂,⁴³ Er-RuO₂,⁴⁰ Ru_{0.8}Cr_{0.2}O_x,³³ Ru_{0.9}Nb_{0.1}O₂,³² Ni-RuO₂,⁸ RuFe@CF₃,⁴⁵ SnRuO_x,³⁹ ZnRuO_x,⁴⁶ SS Pt-RuO₂,¹² Ir₃Ni NCs,⁴⁷ IrO₂@TaB₂,⁴² Ir/D-ATO,⁴⁸ M-RuIrFeCoNiO₂,⁴⁹ Ir-MnO₂(γ),⁴¹ TS-Ir/MnO₂,⁴⁴ Ba_{0.3}(SO₄)_δW_{0.2}Ru_{0.5}O_{2-δ},⁵⁰ La- and Mn-codoped porous cobalt spinel fibers,⁵¹ and CoWO₄.⁵² Green markers represent Ir-based catalysts and blue markers represent non-Ir-based catalysts. Tests were conducted at 80 °C using DI water, unless specified otherwise. The purple region highlights catalysts achieving both long stability hours (>500 h) and high current densities (>0.5 A/cm²).

with enhanced sampling are needed to study redox reactions and catalyst reconstruction under the influence of applied potential and local reaction environments.^{37,38}

PEMWE Studies. The optimized Ru₅₂Co₃₃Mn₉Cr₆ oxide catalyst was integrated into a membrane electrode assembly (MEA) as the anode catalyst for a PEMWE. Commercial IrO₂, commercial RuO₂, and homemade RuO₂ were employed as references. The Ru₅₂Co₃₃Mn₉Cr₆ oxide catalyst exhibited significantly superior activity compared to the RuO₂ and IrO₂ catalysts (Figure 5a). At 80 °C, the cell voltage required to realize a current density of 1 A/cm² was only 1.583 V, outperforming homemade RuO₂ with a similar size prepared using the same method (1.610 V), commercial RuO₂ (1.635 V) (Figure S32), and commercial IrO₂ (1.634 V). Impressively, the Ru₅₂Co₃₃Mn₉Cr₆ oxide catalyst exhibited high current densities of 3 and 4 A/cm² at low cell voltages of 1.772 and 1.858 V, respectively, exceeding the DOE 2026 target (1.8 V at 3 A/cm²)⁵³ and representing one of the most active Ru-based anode catalysts for PEMWE (Figure 5f). The mass activity of the Ru₅₂Co₃₃Mn₉Cr₆ oxide catalyst at 1.5 V was 0.27 A/mg_{Ru}, higher than those of homemade RuO₂ (0.24 A/mg_{Ru}), and commercial IrO₂ (0.17 A/mg_{Ir}) catalysts (Figure 5b). In addition to superior activity, the Ru₅₂Co₃₃Mn₉Cr₆ oxide catalyst showed excellent durability, operating stably for 523 h at 80 °C and 1 A/cm² with an average degradation rate of only 40 μV/h. It also maintained stability for 1037 h at 50 °C and 1 A/cm² with an average degradation rate of 57 μV/h, which competes favorably with reported Ir-based and Ru-based catalysts. In contrast, the voltage increased to 2 V within 20 h for RuO₂ at 50 and 80 °C (Figure 5d). To further understand the degradation of the MEA, polarization curves were used to evaluate catalyst performance over time (Figure 5c). Voltage loss was analyzed at 100 mA/cm² (the kinetic region where the catalyst plays a critical role) and at 1 A/cm². Over 350 h of operation, the voltage losses at 100 mA/cm² and 1 A/cm² were small and nearly identical (13 and 15 mV, respectively). However, at 450 h, the difference in voltage loss grew (27 mV at 100 mA/cm² versus 44 mV at 1 A/cm²), suggesting that the MEA performance degradation could not be fully attributed to anode catalyst degradation alone. Instead, membrane degradation and cathode catalyst poisoning were likely contributing factors to the increased MEA degradation. To evaluate its operational stability under industrially relevant conditions, we conducted a durability test at 3 A/cm² (Figure 5e). The Ru₅₂Co₃₃Mn₉Cr₆ oxide catalyst exhibited stable performance over 220 h with a low voltage decay rate of approximately 10 μV/h. Electrochemical impedance spectroscopy (EIS) was used to evaluate internal resistances and charge transfer dynamics before and after durability testing. For the MEA operated at 1 A/cm² over 1000 h, the high-frequency resistance (HFR) remained relatively stable, decreasing slightly from 230 to 220 mΩ·cm², which may be due to the membrane

activation or instrument variability (Figure S33a). However, the charge transfer resistance (R_{CT}) increased by approximately 30 mΩ·cm² (Figure S33a), which contributed to the potential loss. Interestingly, the MEA tested at 3 A/cm² for 220 h showed negligible changes in HFR, R_{CT}, and ECSA (Figures S33b and S34). Overall, the Ru₅₂Co₃₃Mn₉Cr₆ oxide catalyst demonstrated simultaneous high activity and stability. It exhibited a remarkably low cell voltage (Figure 5f and Table S5) as compared with reported Ir-based and Ru-based catalysts and the longest operational stability reported for a Ru-containing OER catalyst at 1 A/cm² and 80 °C (Figure 5g and Table S5). It is noteworthy that the performance degradation and Ru dissolution of RuO₂ are significantly more pronounced at 80 °C compared to 50 °C, further highlighting the exceptional stability of the Ru₅₂Co₃₃Mn₉Cr₆ oxide catalyst (Figure S35). Looking forward, a commercial PEMWE requires significantly lower degradation rates (e.g., ~5 μV/h) at elevated current densities (e.g., 3 A/cm²). The megalibrary platform introduced here offers a scalable and versatile framework for simultaneously optimizing activity and durability in future catalyst discovery efforts.

CONCLUSIONS

This work shows how megalibraries can dramatically accelerate the pace of discovery of new and functional materials that are nonobvious and, in many cases, not yet contemplated. In this case, Ru₅₂Co₃₃Mn₉Cr₆ oxide was identified as a low cost (~1/16 that of Ir) potential replacement for IrO₂ for the OER. The strong correlation between the activity of nanoparticle catalysts identified using megalibraries and the scaled-up versions of these catalysts is notable and bodes well for using megalibraries to discover promising new catalysts for other reactions. Finally, the extensive data generated by these libraries is unprecedentedly large and will be useful for developing AI and machine learning algorithms that can identify key catalyst design features for specific reactions and further reduce materials cost.

ASSOCIATED CONTENT

Supporting Information

The Supporting Information is available free of charge at <https://pubs.acs.org/doi/10.1021/jacs.5c08326>.

Detailed experimental procedures, materials list, and methods. DFT calculations; additional materials characterization including SEM images, STEM images, EDX maps, EDX spectra, XPS spectra, and XRD data (DOCX)

AUTHOR INFORMATION

Corresponding Authors

Edward H. Sargent — Department of Chemistry, Northwestern University, Evanston, Illinois 60208, United States;

International Institute for Nanotechnology, Evanston, Illinois 60208, United States; Department of Materials Science and Engineering and Department of Electrical and Computer Engineering, Northwestern University, Evanston, Illinois 60208, United States; Email: ted.sargent@northwestern.edu

Chad A. Mirkin – Department of Chemistry, Northwestern University, Evanston, Illinois 60208, United States; International Institute for Nanotechnology, Evanston, Illinois 60208, United States; Department of Materials Science and Engineering, Northwestern University, Evanston, Illinois 60208, United States; orcid.org/0000-0002-6634-7627; Email: chadnano@northwestern.edu

Authors

Jin Huang – Department of Chemistry, Northwestern University, Evanston, Illinois 60208, United States; International Institute for Nanotechnology, Evanston, Illinois 60208, United States; orcid.org/0000-0002-2882-2634

Zhe Wang – Department of Chemistry, Northwestern University, Evanston, Illinois 60208, United States; International Institute for Nanotechnology, Evanston, Illinois 60208, United States

Jiashun Liang – Department of Energy, Environmental & Chemical Engineering, Washington University in St. Louis, St. Louis, Missouri 63130, United States; orcid.org/0000-0003-4328-1650

Xiao-Yan Li – Department of Chemistry, Northwestern University, Evanston, Illinois 60208, United States

Jacob Pietryga – International Institute for Nanotechnology, Evanston, Illinois 60208, United States; Department of Materials Science and Engineering, Northwestern University, Evanston, Illinois 60208, United States

Zihao Ye – Department of Chemistry, Northwestern University, Evanston, Illinois 60208, United States; International Institute for Nanotechnology, Evanston, Illinois 60208, United States; orcid.org/0000-0003-0616-5650

Peter T. Smith – Department of Chemistry, Northwestern University, Evanston, Illinois 60208, United States; International Institute for Nanotechnology, Evanston, Illinois 60208, United States

Alp Kulaksizoglu – International Institute for Nanotechnology, Evanston, Illinois 60208, United States; Department of Materials Science and Engineering, Northwestern University, Evanston, Illinois 60208, United States; orcid.org/0000-0002-6608-8151

Connor R. McCormick – Department of Chemistry, Northwestern University, Evanston, Illinois 60208, United States; International Institute for Nanotechnology, Evanston, Illinois 60208, United States

Jaerim Kim – Department of Chemistry, Northwestern University, Evanston, Illinois 60208, United States

Bosi Peng – Department of Chemistry, Northwestern University, Evanston, Illinois 60208, United States

Zeyan Liu – Department of Chemistry, Northwestern University, Evanston, Illinois 60208, United States

Ke Xie – Department of Chemistry, Northwestern University, Evanston, Illinois 60208, United States; International Institute for Nanotechnology, Evanston, Illinois 60208, United States; orcid.org/0000-0003-4220-272X

Steven B. Torrisi – Energy & Materials Division, Toyota Research Institute, Los Altos, California 94022, United States

Joseph H. Montoya – Energy & Materials Division, Toyota Research Institute, Los Altos, California 94022, United States; orcid.org/0000-0001-5760-2860

Gang Wu – Department of Energy, Environmental & Chemical Engineering, Washington University in St. Louis, St. Louis, Missouri 63130, United States; orcid.org/0000-0003-0885-6172

Complete contact information is available at: <https://pubs.acs.org/10.1021/jacs.5c08326>

Author Contributions

[†]J.H., Z.W., and J.L. contributed equally to this work.

Notes

The authors declare the following competing financial interest(s): C.A.M. has financial interests in Mattiq Inc. and TERA-print LLC, which could potentially benefit from the outcomes of this research. All other authors declare no competing interests.

ACKNOWLEDGMENTS

This material is based on research sponsored by the Toyota Research Institute, Inc., Mattiq, Inc., the U.S. Army DEVCOM ARL Army Research Office (ARO) Energy Sciences Competency (Electrochemistry) Program awards W911NF-23-1-0285 and W911NF-25-2-0018, and the Air Force agreement FA8650-21-2-5028. This project was made possible with the support of Bioindustrial Manufacturing and Design Ecosystem (BioMADE). J.P. gratefully acknowledges support by the National Science Foundation Graduate Research Fellowship Program under grant DGE-2234667. The views and conclusions contained herein are those of the authors and should not be interpreted as necessarily representing the official policies or endorsements, either expressed or implied, of the U.S. Army, U.S. Air Force, the National Science Foundation, the U.S. Government, or BioMADE. The U.S. Government is authorized to reproduce and distribute reprints for Governmental purposes notwithstanding any copyright notation thereon. This work made use of the EPIC, Keck-II, and NUFAB facilities of Northwestern University's NUANCE Center, which has received support from the Soft and Hybrid Nanotechnology Experimental (SHyNE) Resource (NSF ECCS-2025633), the International Institute for Nanotechnology (NIH-S10OD026871), and Northwestern's MRSEC program of the National Science Foundation (NSF DMR-1720139). This work made use of the IMSERC Physical Characterization facility at Northwestern University which has received support from the SHyNE Resource and Northwestern University, the Jerome B. Cohen X-ray Diffraction Facility supported by Northwestern's MRSEC program at the Materials Research Center of Northwestern University, and the SHyNE Resource, and the Northwestern University Quantitative Bioelement Imaging Center supported by the Chicago Biomedical Consortium with support from the Searle Funds at The Chicago Community Trust and supported by the Office Of The Director, National Institutes of Health of the National Institutes of Health (S10OD020118). This manuscript is the result of funding in whole or in part by the National Institutes of Health (NIH). It is subject to the NIH Public Access Policy. Through acceptance of this federal funding, NIH has been given a right to make this manuscript publicly available in PubMed Central upon the Official Date of Publication, as defined by NIH. This research used resources

of the Advanced Photon Source (beamline 12-BM), a U.S. DOE Office of Science User Facility, operated for the DOE Office of Science by Argonne National Laboratory under Contract No. DE-AC02-06CH11357. DFT calculations were performed using computational resources and staff support provided by the Quest high-performance computing facility at Northwestern University, jointly supported by the Office of the Provost, the Office of Research, and Northwestern University Information Technology. Dr. Gang Wu thanks the start-up fund from the Washington University in St. Louis. We thank Mattiq Inc. for the preparation of the 3D-printed SDC head. We thank Dr. Jordan H. Swisher for the help on SDC measurement. We thank Dr. Qiang Sun for the suggestions on MEA fabrication and test. We thank Dr. Hongmin An for the help on DEMS test. We thank Dr. Pengfei Ou for help with DFT calculations. We thank Dr. Jiantao Li for his help with XAS measurements and Dr. Qingying Jia for his guidance on the XAS data analysis.

REFERENCES

- (1) Panchenko, V. A.; Daus, Y. V.; Kovalev, A. A.; Yudaev, I. V.; Litt, Y. V. Prospects for the production of green hydrogen: Review of countries with high potential. *Int. J. Hydrogen Energy* **2023**, *48* (12), 4551–4571.
- (2) Kumar, S. S.; Himabindu, V. Hydrogen production by PEM water electrolysis—A review. *Mater. Sci. Energy Technol.* **2019**, *2* (3), 442–454.
- (3) An, L.; Wei, C.; Lu, M.; Liu, H. W.; Chen, Y. B.; Scherer, G. G.; Fisher, A. C.; Xi, P. X.; Xu, Z. C. J.; Yan, C. H. Recent development of oxygen evolution electrocatalysts in acidic environment. *Adv. Mater.* **2021**, *33* (20), No. 2006328.
- (4) Clapp, M.; Zalitis, C. M.; Ryan, M. Perspectives on current and future iridium demand and iridium oxide catalysts for PEM water electrolysis. *Catal. Today* **2023**, *420*, No. 114140.
- (5) Chen, F.-Y.; Wu, Z.-Y.; Adler, Z.; Wang, H. Stability Challenges of Electrocatalytic Oxygen Evolution Reaction: From Mechanistic Understanding to Reactor Design. *Joule* **2021**, *5* (7), 1704–1731.
- (6) Tian, Y.; Wang, S.; Velasco, E.; Yang, Y.; Cao, L.; Zhang, L.; Li, X.; Lin, Y.; Zhang, Q.; Chen, L. A Co-doped nanorod-like RuO₂ electrocatalyst with abundant oxygen vacancies for acidic water oxidation. *Science* **2020**, *23* (1), No. 100756.
- (7) Wang, J.; Ji, Y.; Yin, R.; Li, Y.; Shao, Q.; Huang, X. Transition metal-doped ultrathin RuO₂ networked nanowires for efficient overall water splitting across a broad pH range. *J. Mater. Chem. A* **2019**, *7* (11), 6411–6416.
- (8) Wu, Z.-Y.; Chen, F.-Y.; Li, B.; Yu, S.-W.; Finckel, Y. Z.; Meira, D. M.; Yan, Q.-Q.; Zhu, P.; Chen, M.-X.; Song, T.-W.; et al. Non-iridium-based electrocatalyst for durable acidic oxygen evolution reaction in proton exchange membrane water electrolysis. *Nat. Mater.* **2023**, *22* (1), 100–108.
- (9) Chen, S.; Huang, H.; Jiang, P.; Yang, K.; Diao, J. F.; Gong, S. P.; Liu, S.; Huang, M. X.; Wang, H.; Chen, Q. W. Mn-doped RuO₂ nanocrystals as highly active electrocatalysts for enhanced oxygen evolution in acidic media. *ACS Catal.* **2020**, *10* (2), 1152–1160.
- (10) Pascuzzi, M. E. C.; Goryachev, A.; Hofmann, J. P.; Hensen, E. J. M. Mn promotion of rutile TiO₂-RuO₂ anodes for water oxidation in acidic media. *Appl. Catal., B* **2020**, *261*, No. 118225.
- (11) Lin, Y.; Tian, Z.; Zhang, L.; Ma, J.; Jiang, Z.; Deibert, B. J.; Ge, R.; Chen, L. Chromium-ruthenium oxide solid solution electrocatalyst for highly efficient oxygen evolution reaction in acidic media. *Nat. Commun.* **2019**, *10* (1), No. 162.
- (12) Wang, J.; Yang, H.; Li, F.; Li, L.; Wu, J.; Liu, S.; Cheng, T.; Xu, Y.; Shao, Q.; Huang, X. Single-site Pt-doped RuO₂ hollow nanospheres with interstitial C for high-performance acidic overall water splitting. *Sci. Adv.* **2022**, *8* (9), No. eabl9271.
- (13) Du, K.; Zhang, L.; Shan, J.; Guo, J.; Mao, J.; Yang, C.-C.; Wang, C.-H.; Hu, Z.; Ling, T. Interface engineering breaks both stability and activity limits of RuO₂ for sustainable water oxidation. *Nat. Commun.* **2022**, *13* (1), No. 5448.
- (14) Bhowmik, T.; Kundu, M. K.; Barman, S. Growth of one-dimensional RuO₂ nanowires on g-Carbon nitride: An active and stable bifunctional electrocatalyst for hydrogen and oxygen evolution reactions at all pH values. *ACS Appl. Mater. Interfaces* **2016**, *8* (42), 28678–28688.
- (15) Laha, S.; Lee, Y.; Podjaski, F.; Weber, D.; Duppe, V.; Schoop, L. M.; Pielhofer, F.; Scheurer, C.; Müller, K.; Starke, U.; et al. Ruthenium oxide nanosheets for enhanced oxygen evolution catalysis in acidic medium. *Adv. Energy Mater.* **2019**, *9* (15), No. 1803795.
- (16) Baik, C.; Lee, S. W.; Pak, C. Control of the pore size distribution inside the RuO₂ catalyst by using silica nanosphere particle for highly efficient water electrolysis. *Microporous Mesoporous Mater.* **2020**, *309*, No. 110567.
- (17) Reddington, E.; Sapienza, A.; Gurau, B.; Viswanathan, R.; Sarangapani, S.; Smotkin, E. S.; Mallouk, T. E. Combinatorial electrochemistry: A highly parallel, optical screening method for discovery of better electrocatalysts. *Science* **1998**, *280* (5370), 1735–1737.
- (18) Danielson, E.; Devenney, M.; Giaquinta, D. M.; Golden, J. H.; Haushalter, R. C.; McFarland, E. W.; Poojary, D. M.; Reaves, C. M.; Weinberg, W. H.; Wu, X. D. A rare-earth phosphor containing one-dimensional chains identified through combinatorial methods. *Science* **1998**, *279* (5352), 837–839.
- (19) Li, M. X.; Zhao, S. F.; Lu, Z.; Hirata, A.; Wen, P.; Bai, H. Y.; Chen, M. W.; Schroers, J.; Liu, Y. H.; Wang, W. H. High-temperature bulk metallic glasses developed by combinatorial methods. *Nature* **2019**, *569* (7754), 99–103.
- (20) Haber, J. A.; Cai, Y.; Jung, S. H.; Xiang, C. X.; Mitrovic, S.; Jin, J.; Bell, A. T.; Gregoire, J. M. Discovering Ce-rich oxygen evolution catalysts, from high throughput screening to water electrolysis. *Energy Environ. Sci.* **2014**, *7* (2), 682–688.
- (21) Gregoire, J. M.; Zhou, L.; Haber, J. A. Combinatorial synthesis for AI-driven materials discovery. *Nat. Synth.* **2023**, *2* (6), 493–504.
- (22) Klunder, E. J.; Hedrick, J. L.; Brown, K. A.; Rao, R.; Meckes, B.; Du, J. S. S.; Moreau, L. M.; Maruyama, B.; Mirkin, C. A. Catalyst discovery through megalibraries of nanomaterials. *Proc. Natl. Acad. Sci. U.S.A.* **2019**, *116* (1), 40–45.
- (23) Huo, F. W.; Zheng, Z. J.; Zheng, G. F.; Giam, L. R.; Zhang, H.; Mirkin, C. A. Polymer pen lithography. *Science* **2008**, *321* (5896), 1658–1660.
- (24) Chai, J.; Huo, F.; Zheng, Z.; Giam, L. R.; Shim, W.; Mirkin, C. A. Scanning probe block copolymer lithography. *Proc. Natl. Acad. Sci. U.S.A.* **2010**, *107* (47), 20202–20206.
- (25) Smith, P. T.; Ye, Z. H.; Pietryga, J.; Huang, J.; Wahl, C. B.; Orbeck, J. K. H.; Mirkin, C. A. Molecular thin films enable the synthesis and screening of nanoparticle megalibraries containing millions of catalysts. *J. Am. Chem. Soc.* **2023**, *145* (25), 14031–14043.
- (26) Lai, M. L.; Shin, D.; Jibril, L.; Mirkin, C. A. Combinatorial synthesis and screening of mixed halide perovskite megalibraries. *J. Am. Chem. Soc.* **2022**, *144* (30), 13823–13830.
- (27) Wahl, C. B.; Aykol, M.; Swisher, J. H.; Montoya, J. H.; Suram, S. K.; Mirkin, C. A. Machine learning-accelerated design and synthesis of polyelemental heterostructures. *Sci. Adv.* **2021**, *7* (52), No. eabj5505.
- (28) Lin, C.; Li, J.-L.; Li, X.; Yang, S.; Luo, W.; Zhang, Y.; Kim, S.-H.; Kim, D.-H.; Shinde, S. S.; Li, Y.-F.; et al. In-situ reconstructed Ru atom array on α -MnO₂ with enhanced performance for acidic water oxidation. *Nat. Catal.* **2021**, *4* (12), 1012–1023.
- (29) Piner, R. D.; Zhu, J.; Xu, F.; Hong, S. H.; Mirkin, C. A. "Dip-pen" nanolithography. *Science* **1999**, *283* (5402), 661–663.
- (30) Biesinger, M. C.; Payne, B. P.; Grosvenor, A. P.; Lau, L. W. M.; Gerson, A. R.; Smart, R. S. C. Resolving surface chemical states in XPS analysis of first row transition metals, oxides and hydroxides: Cr, Mn, Fe, Co and Ni. *Appl. Surf. Sci.* **2011**, *257* (7), 2717–2730.
- (31) Geiger, S.; Kasian, O.; Ledendecker, M.; Pizzutillo, E.; Mingers, A. M.; Fu, W. T.; Diaz-Morales, O.; Li, Z.; Oellers, T.; Fruchter, L.

et al. The stability number as a metric for electrocatalyst stability benchmarking. *Nat. Catal.* **2018**, *1* (7), 508–515.

(32) Liu, H.; Zhang, Z.; Fang, J. J.; Li, M. X.; Sendeku, M. G.; Wang, X.; Wu, H. Y.; Li, Y. P.; Ge, J. J.; Zhuang, Z. B.; et al. Eliminating over-oxidation of ruthenium oxides by niobium for highly stable electrocatalytic oxygen evolution in acidic media. *Joule* **2023**, *7* (3), 558–573.

(33) Shen, Y.; Zhang, X.-L.; Qu, M.-R.; Ma, J.; Zhu, S.; Min, Y.-L.; Gao, M.-R.; Yu, S.-H. Cr dopant mediates hydroxyl spillover on RuO₂ for high-efficiency proton exchange membrane electrolysis. *Nat. Commun.* **2024**, *15* (1), No. 7861.

(34) Wang, Y.; Lei, X.; Zhang, B.; Bai, B.; Das, P.; Azam, T.; Xiao, J. P.; Wu, Z. S. Breaking the Ru-O-Ru symmetry of a RuO catalyst for sustainable acidic water oxidation. *Angew. Chem., Int. Ed.* **2024**, *63* (3), No. e202316903.

(35) George, J.; Petretto, G.; Naik, A.; Esters, M.; Jackson, A. J.; Nelson, R.; Dronskowski, R.; Rignanese, G. M.; Hautier, G. Automated bonding analysis with crystal orbital Hamilton populations. *ChemPlusChem* **2022**, *87* (11), No. e202200123.

(36) Wang, L. Q.; Hung, S. F.; Zhao, S.; Wang, Y.; Bi, S. W.; Li, S. X.; Ma, J. J.; Zhang, C. C.; Zhang, Y.; Li, L. L.; et al. Modulating the covalency of Ru-O bonds by dynamic reconstruction for efficient acidic oxygen evolution. *Nat. Commun.* **2025**, *16* (1), No. 3502, DOI: 10.1038/s41467-025-58654-0.

(37) Nong, H. N.; Falling, L. J.; Bergmann, A.; Klingenhof, M.; Tran, H. P.; Spöri, C.; Mom, R.; Timoshenko, J.; Zichittella, G.; Knop-Gericke, A.; et al. Key role of chemistry versus bias in electrocatalytic oxygen evolution. *Nature* **2020**, *587* (7834), 408–413.

(38) Pessemesse, Q.; Perochon, A.; Copéret, C.; Perrin, M.-E. L.; Payard, P.-A. Alloy reorganization and dynamics in group-10-metal-gallium nanoparticles under reactive atmospheres: impact on local environment and reactivity. *J. Am. Chem. Soc.* **2025**, *147* (26), 22498–22508.

(39) Shi, Z.; Li, J.; Wang, Y.; Liu, S.; Zhu, J.; Yang, J.; Wang, X.; Ni, J.; Jiang, Z.; Zhang, L.; et al. Customized reaction route for ruthenium oxide towards stabilized water oxidation in high-performance PEM electrolyzers. *Nat. Commun.* **2023**, *14* (1), No. 843.

(40) Li, L.; Zhang, G.; Zhou, C.; Lv, F.; Tan, Y.; Han, Y.; Luo, H.; Wang, D.; Liu, Y.; Shang, C.; et al. Lanthanide-regulating Ru-O covalency optimizes acidic oxygen evolution electrocatalysis. *Nat. Commun.* **2024**, *15* (1), No. 4974.

(41) Li, A.; Kong, S.; Adachi, K.; Ooka, H.; Fushimi, K.; Jiang, Q.; Ofuchi, H.; Hamamoto, S.; Oura, M.; Higashi, K.; et al. Atomically dispersed hexavalent iridium oxide from MnO₂ reduction for oxygen evolution catalysis. *Science* **2024**, *384* (6696), 666–670.

(42) Wang, Y.; Zhang, M.; Kang, Z.; Shi, L.; Shen, Y.; Tian, B.; Zou, Y.; Chen, H.; Zou, X. Nano-metal diborides-supported anode catalyst with strongly coupled TaO_x/IrO₂ catalytic layer for low-iridium-loading proton exchange membrane electrolyzer. *Nat. Commun.* **2023**, *14* (1), No. 5119.

(43) Zhou, C.; Li, L.; Dong, Z.; Lv, F.; Guo, H.; Wang, K.; Li, M.; Qian, Z.; Ye, N.; Lin, Z.; et al. Pinning effect of lattice Pb suppressing lattice oxygen reactivity of Pb-RuO₂ enables stable industrial-level electrolysis. *Nat. Commun.* **2024**, *15* (1), No. 9774.

(44) Su, H.; Yang, C.; Liu, M.; Zhang, X.; Zhou, W.; Zhang, Y.; Zheng, K.; Lian, S.; Liu, Q. Tensile straining of iridium sites in manganese oxides for proton-exchange membrane water electrolyzers. *Nat. Commun.* **2024**, *15* (1), No. 95.

(45) Chen, J.; Ma, Y.; Huang, T.; Jiang, T.; Park, S.; Xu, J.; Wang, X.; Peng, Q.; Liu, S.; Wang, G.; Chen, W. Ruthenium-based binary alloy with oxide nanosheath for highly efficient and stable oxygen evolution reaction in acidic media. *Adv. Mater.* **2024**, *36* (26), No. 2312369.

(46) Sun, P.; Qiao, Z.; Dong, X.; Jiang, R.; Hu, Z.-T.; Yun, J.; Cao, D. Designing 3d transition metal cation-doped MRuO_x as durable acidic oxygen evolution electrocatalysts for PEM water electrolyzers. *J. Am. Chem. Soc.* **2024**, *146* (22), 15515–15524.

(47) Ding, H.; Su, C.; Wu, J.; Lv, H.; Tan, Y.; Tai, X.; Wang, W.; Zhou, T.; Lin, Y.; Chu, W.; et al. Highly crystalline iridium–nickel

nanocages with subnanopores for acidic bifunctional water splitting electrolysis. *J. Am. Chem. Soc.* **2024**, *146* (11), 7858–7867.

(48) Lee, G. R.; Kim, J.; Hong, D.; Kim, Y. J.; Jang, H.; Han, H. J.; Hwang, C.-K.; Kim, D.; Kim, J. Y.; Jung, Y. S. Efficient and sustainable water electrolysis achieved by excess electron reservoir enabling charge replenishment to catalysts. *Nat. Commun.* **2023**, *14* (1), No. 5402.

(49) Hu, C.; Yue, K.; Han, J.; Liu, X.; Liu, L.; Liu, Q.; Kong, Q.; Pao, C.-W.; Hu, Z.; Suenaga, K.; et al. Misoriented high-entropy iridium ruthenium oxide for acidic water splitting. *Sci. Adv.* **2023**, *9* (37), No. eadf9144.

(50) Xue, Y.; Zhao, J.; Huang, L.; Lu, Y.-R.; Malek, A.; Gao, G.; Zhuang, Z.; Wang, D.; Yavuz, C. T.; Lu, X. Stabilizing ruthenium dioxide with cation-anchored sulfate for durable oxygen evolution in proton-exchange membrane water electrolyzers. *Nat. Commun.* **2023**, *14* (1), No. 8093.

(51) Chong, L.; Gao, G.; Wen, J.; Li, H.; Xu, H.; Green, Z.; Sugar, J. D.; Kropf, A. J.; Xu, W.; Lin, X.-M.; et al. La- and Mn-doped cobalt spinel oxygen evolution catalyst for proton exchange membrane electrolysis. *Science* **2023**, *380* (6645), 609–616.

(52) Ram, R.; Xia, L.; Benzidi, H.; Guha, A.; Golovanova, V.; Manjón, A. G.; Rauret, D. L.; Berman, P. S.; Dimitropoulos, M.; Mundet, B.; et al. Water-hydroxide trapping in cobalt tungstate for proton exchange membrane water electrolysis. *Science* **2024**, *384* (6702), 1373–1380.

(53) Pivovar, B. H2NEW: Hydrogen (H2) from Next-Generation Electrolyzers of Water Overview, 2023. <https://www.nrel.gov/docs/fy23osti/86490.pdf>. (accessed July 04, 2025).



CAS BIOFINDER DISCOVERY PLATFORM™

**CAS BIOFINDER
HELPS YOU FIND
YOUR NEXT
BREAKTHROUGH
FASTER**

Navigate pathways, targets, and
diseases with precision

Explore CAS BioFinder

CAS
A division of the
American Chemical Society